Depth-discriminative Metric Learning for Monocular 3D Object Detection

Wonhyeok Choi[*]   **Mingyu Shin**[*]   **Sunghoon Im**[†]

DGIST, Daegu, Korea

{smu06117, alsrb4446, sunghoonim}@dgist.ac.kr

Abstract

Monocular 3D object detection poses a significant challenge due to the lack of depth information in RGB images. Many existing methods strive to enhance the object depth estimation performance by allocating additional parameters for object depth estimation, utilizing extra modules or data. In contrast, we introduce a novel metric learning scheme that encourages the model to extract depth-discriminative features regardless of the visual attributes without increasing inference time and model size. Our method employs the distance-preserving function to organize the feature space manifold in relation to ground-truth object depth. The proposed (K, B, ϵ)-quasi-isometric loss leverages predetermined pairwise distance restriction as guidance for adjusting the distance among object descriptors without disrupting the non-linearity of the natural feature manifold. Moreover, we introduce an auxiliary head for object-wise depth estimation, which enhances depth quality while maintaining the inference time. The broad applicability of our method is demonstrated through experiments that show improvements in overall performance when integrated into various baselines. The results show that our method consistently improves the performance of various baselines by 25.27% and 4.54% on average across KITTI and Waymo, respectively.

1   Introduction

Monocular 3D object detections [21, 24, 25, 29] has gained prominence as a cost-effective and easily deployable solution, playing a critical role in autonomous driving and robotic navigation systems. Typically, the frameworks consist of a feature extractor and lightweight multi-head architectures that predict the projected centers, depths, bounding box sizes, and heading directions of multiple objects from a single RGB image [19, 21, 24, 25, 28, 29, 44]. Among these tasks, object depth estimation, inferring the distance from a monocular camera to the center of an object, is the most challenging sub-task due to depth ambiguity. Previous work [25] has highlighted this issue in ablation studies, revealing that substituting object depth predictions with ground-truth (GT) values significantly improves overall performance, while replacing other sub-tasks, such as heading direction and 3D size, does not notably enhance performance. Furthermore, several prior works [3, 10, 19, 24, 29, 30, 39, 44] have attempted to improve object depth estimation quality by adding additional modules or introducing new formulations. However, despite the subsequent increase in inference time and model size, the improvement in performance remains limited.

These observations suggest that monocular 3D object detection heavily relies on object depth quality; nevertheless, conventional methods yield unsatisfactory results due to the extraction of less-discriminative features for object depth inference. One reason is that the extracted feature involves visual attributes, such as the color, size, and heading direction of objects, resulting in the object

---

[*]Equal Contribution

[†]Corresponding Author

depth head receiving feature with limited depth discernment. To improve object depth performance, the network should be capable of extracting purely depth-discriminative features that involve essential geometric information, irrespective of the visual attribute. A feasible method for extracting the depth-discriminative features involves using deep metric learning schemes such as contrastive learning [6, 7, 42] or representation learning [5, 36].

However, most existing deep metric learning schemes [6, 7, 16, 42] rely on aggressive two-view augmentation (*i.e.* Affine transform) to train the distance or similarity metric. This aggressive data augmentation method is hardly leveraged in current monocular 3D object detection frameworks due to the violation of geometric constraints, where horizontal flip and color distortion are the only two methods used in this field for a long time [20]. One alternative way is to learn a regression-aware representation by contrasting samples against each other based on their target distance using GT labels [42]. However, forcibly arranging the manifold of the feature space using this depth distance metric may negatively impact the performance of the other tasks, because the feature extractor for monocular 3D object detection inevitably produces complex shared representations across multiple sub-tasks. Note that the experiment of negative impact is conducted in Sec. 5.2.

To address these issues, we propose a (K, B, ϵ)-quasi-isometric loss, a new metric learning approach that encourages the network to extract depth-discriminative features using object depth labels. Inspired by several manifold learning schemes [31, 35], we locally preserve the neighborhood distances to maintain the natural non-linear manifold of feature space in order to mitigate the negative transfer effect on other sub-tasks. Our approach utilizes the quasi-isometric properties providing a relaxed condition for the distance metric between the depth and feature metric spaces. This enables the model to arrange the feature space with respect to the object depth labels while maintaining the performance of other sub-tasks. Moreover, we introduce an auxiliary head for object-wise depth estimation to further improve object depth estimation. The head component is removed after the training process, ensuring that the inference time remains unaffected and does not experience an increase. Experimental results indicate that the proposed method consistently outperforms state-of-the-art baselines across a variety of 3D object detection datasets. Our method has been shown to be compatible with various monocular 3D object detection frameworks [15, 21, 24, 25, 29], demonstrating its broad applicability without compromising inference time or increasing model size. The effectiveness of each proposed module is further underscored through comprehensive ablation studies.

Our contributions can be summarized as follows:

- We propose a simple yet effective metric learning scheme that preserves the geodesic distance of depth information to feature space.

- We present an auxiliary head for object-wise depth estimation, which enhances the depth quality without impacting the inference time, maintaining efficient performance.

- Our method significantly enhances the performance of various monocular 3D object detection methods without increasing inference time and model size.

2   Related work

Monocular 3D object detection.   Monocular 3D object detection can be broadly categorized into two types. The first type [3, 19, 21, 24, 25, 27, 39, 44] predicts the localization of objects of interest around an ego vehicle using only RGB images, annotations, and camera calibrations. Most of them are based on CenterNet [46]. They are divided into several sub-tasks, with a primary focus on estimating accurate object depth. The works [24] and [44] propose the formulations of object depth estimation. MonoCon [21] leverages the abundant contexts in conventional 3D bounding box annotations to integrate various auxiliary tasks. The second category leverages additional data, such as pre-trained models [8, 10, 15, 29, 30, 37] or CAD models [26, 40], to compensate for the lack of 3D information in monocular images. Some prior works utilize pre-trained depth estimators to address the lack of depth information, either by converting the monocular setups to LiDAR/Stereo environments [8, 37] or by allocating more parameters to the depth estimation task [10, 15, 43]. Alternatively, certain methods employ completed depth maps from pre-trained depth completion models [29] or pre-trained LiDAR-based detectors [8, 14] to supervise their models. Notably, DID-M3D [29] divides object depth into visual and attribute depth using completed depth maps to address the ambiguity of the object depth.

Manifold geometry preservation. Deep learning networks, consisting of continuous and differentiable (precisely, almost everywhere differentiable) layers, ensure smooth mapping of networks $f : \mathbb{R}^m \to \mathbb{R}^n$. This guarantees that neighborhoods in $\mathbb{R}^m$ will be mapped into neighborhoods in the embedding space $\mathbb{R}^n$ with some amount of "stretching" and vice versa. Manifold learning has been studied to preserve most or all of the essential information by minimizing these stretches. Many works [1, 2, 18, 31, 45] aim to create meaningful representations when embedding high-dimensional data into lower dimensions. The traditional linear embedding algorithms commonly use the matrix decomposition to preserve the original variance[1] or pairwise distance [18]. More recent algorithms [2, 31, 35, 45] construct the neighborhood graphs by preprocessing the dataset using ϵ-ball or k-nearest neighbors for each point, embedding the data while preserving the neighbor samples' distance. In particular, Isomap [35] estimates the shortest path in the neighborhood graph between every pair of data points and then employs the Euclidean Multidimensional Scaling (MDS) algorithm [18] to embed the points in d dimensions with minimum distance distortion all at once. These non-linear embedding algorithms can account for the non-linear nature of the manifold by preserving the distance between neighborhood samples.

Metric learning. Metric learning is one of the machine learning techniques that aims to learn an effective distance metric between data points by using training data. To achieve this, methods such as [6, 7, 16] attempt to minimize the distance between samples from the same class while maximizing the distance between samples from different classes. These methods demonstrate improved performance for self-supervised learning by learning in an end-to-end fashion, including two-view augmentation or depending on class labels. These deep metric learning methods typically target classification tasks because the positive/negative pairs are defined as belonging to the same or different classes. More recent works [33, 38, 42] extensively apply metric learning in the context of regression. These works either directly use the target distance to contrast samples against each other [38, 42] or leverage representation learning in a semi-supervised learning scenario [33].

3 Method

Our final goal is to boost the object depth performance by extracting the depth-discriminative features without increasing inference time. Similar to common deep metric learning schemes [6, 7, 42], we propose a loss term that preserves a meaningful low-dimensional data structure in the feature space.

3.1 Preliminary

Metric space. A metric space is a mathematical concept that characterizes a set of points and a function that measures the distance between any two points in the set. Formally, a metric space can be defined as a pair (M, d), where M represents a set and d is a distance function on M. The distance function d must satisfies the following axioms [13] for any three points $x, y, z \in M$:

1. Non-negativity: $d(x, y) \geq 0$ and $d(x, y) = 0$ if and only if $x = y$.
2. Symmetry: $d(x, y) = d(y, x)$ for all $x, y \in M$.
3. Triangle inequality: $d(x, y) \leq d(x, z) + d(z, y)$ for all $x, y, z \in M$.

Quasi-isometry. A quasi-isometry is a function between two metric spaces that preserves distances up to a constant factor, even though it may locally distort angles and distances. Let $\mathcal{Q}$ be a function from one metric space (M_1, d_1) to another metric space (M_2, d_2). $\mathcal{Q}$ is considered a quasi-isometry from (M_1, d_1) to (M_2, d_2) if there exist constants $K \geq 1$, $B \geq 0$, and $\epsilon \geq 0$ such that both of the following properties hold:

1. $\forall x_1, x_2 \in M_1 \;:\; \frac{1}{K} \cdot d_1(x_1, x_2) - B \leq d_2(\mathcal{Q}(x_1), \mathcal{Q}(x_2)) \leq K \cdot d_1(x_1, x_2) + B.$
2. $\forall z \in M_2 \;:\; \exists x \in M_1 \; s.t. \; d_2(z, \mathcal{Q}(x)) \leq \epsilon.$

Quasi-isometry does not necessarily require continuity [4]. This property is advantageous because other distance-preserving transformations may not possess it, and most datasets are finite. Therefore, we use these conditions as constraints to ensure that the feature space retains the geometrical information of the depth metric space.

3.2 Problem Definition

The task of monocular 3D object detection aims to predict both the object class c and the 3D bounding box $\mathbf{b}$ for multiple objects within an image $\mathbf{I}$. Recently, CenterNet [46] has become the best practice for monocular 3D object detection, with subsequent works [19, 21, 24, 25, 29, 44] adopting its pipeline. These methods decompose the bounding box $\mathbf{b} = [X, Y, Z, h, w, l, \gamma]$ estimation problem into separate estimations of the coarse projected 3D center (u, v), the depth of object center z, the center offset $(\delta u, \delta v)$, the 3D size dimensions (h, w, l), and heading direction γ (*i.e.*, the yaw angle). The 3D object center $[X, Y, Z]$ is computed by back-projecting the projected center with the corresponding depth, given the intrinsic matrix of the camera $\mathbf{K}$, as follows:

$$u_c = u + \delta u, \ v_c = v + \delta v,$$
$$[X, Y, Z]^T = \mathbf{K}^{-1}[u_c \cdot z, v_c \cdot z, z]^T. \tag{1}$$

The networks consist of feature extractor $\mathcal{F}_\theta$ and task-specific heads $\mathcal{G}_{\phi^t}$ that produce the feature maps $\mathbf{h}$ and the per-pixel output maps $\tilde{\mathbf{o}}_t$, where $t \in \mathbf{T} = \{t_c, t_u, t_v, t_{\delta u}, t_{\delta v}, t_z, t_h, t_w, t_l, t_\gamma\}$, respectively, as follows:

$$\mathbf{h} = \mathcal{F}_\theta(\mathbf{I}), \ \mathcal{F}_\theta : \mathbb{R}^{3 \times H \times W} \to \mathbb{R}^{C \times H' \times W'},$$
$$\tilde{\mathbf{o}}_t = \mathcal{G}_{\phi^t}(\mathbf{h}), \ \mathcal{G}_{\phi^t} : \mathbb{R}^{C \times H' \times W'} \to \mathbb{R}^{H' \times W'}, \tag{2}$$

where H, W represent the spatial resolution of the image, and C, H', W' denote the channel and spatial resolution of the feature maps, which is downsampled from the image resolution. The final object-wise results $\mathbf{o_T}$ are extracted from the non-learnable function $\mathcal{H}$, given the intermediate per-pixel outputs $\tilde{\mathbf{o}}_{\mathbf{T} = \{t_c, t_u, t_v, t_{\delta u}, t_{\delta v}, t_z, t_h, t_w, t_l, t_\gamma\}}$, as follows:

$$\mathbf{o_T} = \mathcal{H}(\tilde{\mathbf{o}}_\mathbf{T}), \ \mathcal{H} : \mathbb{R}^{|\mathbf{T}| \times H' \times W'} \to \mathbb{R}^{|\mathbf{T}| \times N}, \ N \geq 0, \tag{3}$$

where the number of detected objects N is not fixed and can be zero if no object is detected.

3.3 Methodology

In this paper, our primary focus is on training the feature extractor $\mathcal{F}_\theta$ with the objective of extracting features that enhance the discriminability of object depth. At the same time, we aim to preserve the discriminability of other sub-tasks, such as the projected 3D center, bounding box size, and heading directions. To achieve this, we propose a metric learning method that encourages the network to extract depth-discriminative features by leveraging object depth labels.

Given M training images $\mathbf{I}^i$, where $i \in I = \{1, ..., M\}$, and N^i GT objects in the image $\mathbf{I}^i$, we extract object descriptors $\rho^{(i,j)}$, where $j \in J = \{1, ..., N^i\}$, from feature maps $\mathbf{h}^i$ using GT coarse projected 3D center $u^{(i,j)}, v^{(i,j)}$ and obtain the corresponding GT object depths $z^{(i,j)}$. We build a set of object descriptors $\mathbf{P} = \bigcup_{\{i \in I, \ j \in J\}} \rho^{(i,j)}$ and a set of corresponding object depth $\mathbf{Z} = \bigcup_{\{i \in I, \ j \in J\}} z^{(i,j)}$. We then define two metric spaces $(\mathbf{Z}, d_1)$ and $(\mathbf{P}, d_2)$, where d_1 and d_2 represent the Minkowski distance in Euclidean space (*i.e.*, L1 distance). The finite sets $\mathbf{Z}$ and $\mathbf{P}$ consist of L elements, corresponding to objects in the dataset ($|\mathbf{Z}| = |\mathbf{P}| = L = \sum_{i \in I} N^i$). Consequently, we can establish a one-to-one function $\mathcal{Q}$ between these two metric spaces as follow:

$$\mathcal{Q}(z^l) = \rho^l, \ \mathcal{Q} : \mathbf{Z} \to \mathbf{P}, \ l \in \{1, 2, \ldots, L\}. \tag{4}$$

Our goal is for the function $\mathcal{Q}$ to enforce a quasi-isometric between $\mathbf{Z}$-space and $\mathbf{P}$-space by using the properties of quasi-isometry in Sec. 3.1. This can encourage the network to extract depth-discriminative features in $\mathbf{P}$-space by utilizing object depth labels in $\mathbf{Z}$-space. However, enforcing a quasi-isometric between the low-dimensional $\mathbf{Z}$-space and the high-dimensional $\mathbf{P}$-space can damage the non-linearity of the natural manifold, potentially causing the negative transfer to other sub-tasks. Therefore, we adopt the local distance-preserving condition of the non-linear embedding methods such as Isomap [35] and LLE [31]. The revised version of the quasi-isometry condition is as follows:

(i) $\mathbf{U}_{\check{z}} = \{z \in \mathbf{Z} | z \in \mathcal{B}_{\check{z}, \epsilon}\}$,

(ii) $\forall z_1 \in \mathbf{Z}$, s.t. $\forall z_2 \in \mathbf{U}_{z_1} : \frac{1}{K} \cdot d_1(z_1, z_2) - B \leq d_2(\mathcal{Q}(z_1), \mathcal{Q}(z_2)) \leq K \cdot d_1(z_1, z_2) + B$,

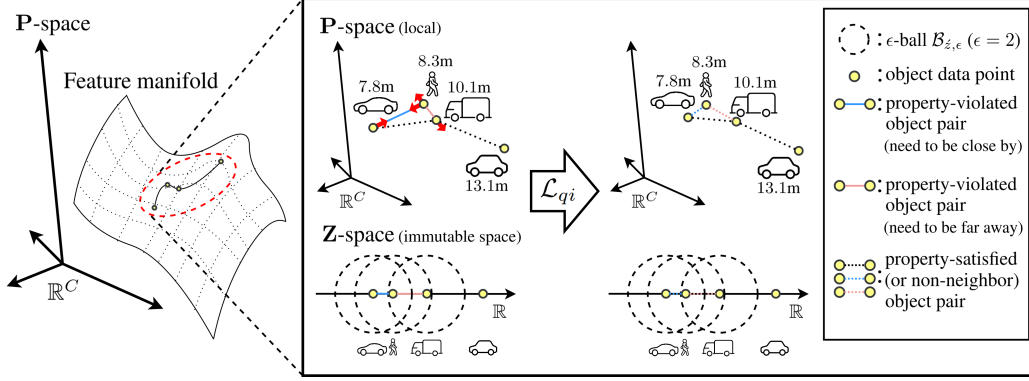(iii) $\forall \rho \in \mathbf{P} : \exists z \in \mathbf{Z}$, s.t. $d_2(\rho, \mathcal{Q}(z)) \leq \epsilon$,

4

Figure 1: Illustration of our quasi-isometric loss $\mathcal{L}_{qi}$.

where $\mathcal{B}_{\acute{z},\epsilon}$ is a ball with radius ϵ centered around $\acute{z}$. By applying the quasi-isometric properties solely to neighboring samples within the ϵ-ball, the non-linearity of the feature manifold is preserved, and the shortest curve distance between any two arbitrary samples on the manifold (*a.k.a.* geodesic) in **P**-space is maintained instead of the Minkowski distance. By ensuring these three conditions (i), (ii), (iii) met for a sufficiently small $K \geq 1$ and $B \geq 0$, we can encourage object features ρ^l to be depth-discriminative using their corresponding object depth z^l. To achieve this, function $\mathcal{Q}$ must satisfy these conditions, which involves training the parameter θ of the feature extractor $\mathcal{F}$.

(K, B, ϵ)-Quasi-isometric loss. We propose a quasi-isometric loss term that enforces the quasi-isometric between the depth and feature metric spaces while preserving the distance among the neighbor data points as illustrated in Fig. 1. In particular, the proposed loss term is designed to arrange **P**-space samples that do not satisfy these conditions. To ensure efficient training within the constraints of limited GPU memory, we use the samples within a mini-batch instead of using the entire input dataset as done in previous works [2, 31, 35]. We selectively choose the neighbor objects in a mini-batch with respect to their corresponding depth labels, where neighboring object depths are within $\mathbf{U}_z$.

Suppose that objects in mini-batch images $\mathbf{I}_b$ correspond to the object depths $\mathbf{Z}_b$ and object features $\mathbf{P}_b$ on **Z**-space and **P**-space, respectively. We can then identify the object feature pair sets $\mathbf{P}_b^+, \mathbf{P}_b^-$ that violate the revised property (ii) by transposing it as follow:

$$\forall (\rho_1, \rho_2) \in \mathbf{P}_b^+ \subset \mathbf{P}_b \times \mathbf{P}_b, \text{ s.t. } |z_1, z_2| \leq \epsilon : d_2(\rho_1, \rho_2) \nleq K \cdot d_1(z_1, z_2) + B, \quad (5a)$$

$$\forall (\rho_1, \rho_2) \in \mathbf{P}_b^- \subset \mathbf{P}_b \times \mathbf{P}_b, \text{ s.t. } |z_1, z_2| \leq \epsilon : \frac{1}{K} \cdot d_1(z_1, z_2) - B \nleq d_2(\rho_1, \rho_2), \quad (5b)$$

where (z_1, z_2) is the corresponding depth pair of the object features (ρ_1, ρ_2). For an object feature pair with distance $d_2(\rho_1, \rho_2)$ in **P**-space, the distance is larger for $\mathbf{P}_b^+$ in Eq. 5a or smaller for $\mathbf{P}_b^-$ in Eq. 5b than the corresponding depth pair distance $d_1(z_1, z_2)$ with a factor of K and the additive constant B. To ensure these property-violating object feature pairs $\mathbf{P}_b^+, \mathbf{P}_b^-$ satisfy the property (ii), we propose the (K, B, ϵ)-quasi-isometry loss, which modifies the Normalized Temperature-Scaled Cross-Entropy loss (NT-Xent loss) from [6] as follows:

$$\mathcal{L}_{qi} = -\frac{1}{|\mathbf{P}_b^+|} \sum_{(\rho_i, \rho_j) \in \mathbf{P}_b^+} \log \frac{\mathrm{S}^+(\rho_i, \rho_j)}{\mathrm{S}^+(\rho_i, \rho_j) + \sum_{(\rho_k, \rho_l) \in \mathbf{P}_b^-} \mathrm{S}^-(\rho_k, \rho_l)},$$

$$\mathrm{S}^+(\rho_i, \rho_j) = \exp(-(\|\rho_i, \rho_j\|_p - K|z_i, z_j| - B)/\tau), \quad (6)$$

$$\mathrm{S}^-(\rho_i, \rho_j) = \exp(-(\frac{1}{K}|z_i, z_j| - B - \|\rho_i, \rho_j\|_p)/\tau),$$

Algorithm 1 (K, B, ϵ)-Quasi-isometric loss

Input: $\mathbf{h}, (u_i, v_i), z_i$, where $i \in \{1, 2, ..., n\}$, n is the number of objects in a batch.

1: $\mathbf{h}_{avg} \leftarrow$ avg_pool_5x5($\mathbf{h}$)   # feature map avg. pool
2: initialize $\mathbf{P} = [\,]$
3: **for** $\forall$ i **do**
4:    $\mathbf{P}[i] = \rho_i = \mathbf{h}_{avg}[:, u_i, v_i]$
5: **end for**
6: $\mathbf{Z} \leftarrow \{z_1, z_2, \ldots, z_n\}$ that correspond to $\mathbf{P}$.
7: $\mathcal{M}_\mathbf{P} \leftarrow \begin{pmatrix} <\rho_1,\rho_1> & <\rho_1,\rho_2> & \cdots & <\rho_1,\rho_n> \\ \vdots & \vdots & \ddots & \vdots \\ <\rho_n,\rho_1> & <\rho_n,\rho_2> & \cdots & <\rho_n,\rho_n> \end{pmatrix},$
                            # where $< a, b >$ is the Minkowski metric $\|a, b\|_p$.
8: $\mathcal{M}_\mathbf{Z} \leftarrow \begin{pmatrix} |z_1,z_1| & |z_1,z_2| & \cdots & |z_1,z_n| \\ \vdots & \vdots & \ddots & \vdots \\ |z_n,z_1| & |z_n,z_2| & \cdots & |z_n,z_n| \end{pmatrix}$
9: $\mathcal{M}^+ \leftarrow \mathcal{M}_\mathbf{P} - K\mathcal{M}_\mathbf{Z} - B$ # To find property-violated object features. (Eq. 5a)
10: $\mathcal{M}^- \leftarrow \frac{1}{K}\mathcal{M}_\mathbf{Z} - \mathcal{M}_\mathbf{P} - B$ # To find property-violated object features. (Eq. 5b)
11: $(\mathcal{M}^+)_{ij} \leftarrow 0$, where $|z_i, z_j| > \epsilon$ or $i \geq j$ or $(\mathcal{M}^+)_{ij} < 0$.
12: $(\mathcal{M}^-)_{ij} \leftarrow 0$, where $|z_i, z_j| > \epsilon$ or $i \geq j$ or $(\mathcal{M}^-)_{ij} < 0$.
13: $\text{ancs}^+ \leftarrow \exp(-\mathcal{M}^+/\tau)$ # τ is temperature term.
14: $\text{ancs}^- \leftarrow \sum(\exp(-\mathcal{M}^-/\tau))$
15: $\mathcal{L}_{qi} = \text{mean}(-\log(\text{ancs}^+/(\text{ancs}^+ + \text{ancs}^- + \delta)))$ # $\delta = 1e - 12$: div. assert

---

where τ is the temperature term, and $\|\cdot, \cdot\|_p$ is p-norm, and $K \geq 1, B \geq 0$ denote the pre-defined hyperparameters that determine the hardness of quasi-isometric property. This loss aims to make the property-violated object features comply with the quasi-isometric property by assuming $\mathbf{P}_b^{+/-}$ as positive/negative anchors, respectively. The similarity metrics $\text{S}^{+/-}$ are always positive values in $(0, 1]$ that imply a negative distance gap between the distance metric on $\mathbf{Z}$-space and $\mathbf{P}$-space. These adjustments are necessary for proper alignment between the two spaces, noting that $\mathbf{P}_b$ is derived from $\mathcal{F}_\theta(\mathbf{I}_b)$.

Object-wise depth map loss.   According to Eq. 1, the estimated object depth $\hat{z}$ and coarse projected 3D center $(\hat{u}, \hat{v})$ jointly determine the location of the object 3D center $(\hat{X}, \hat{Y}, \hat{Z})$. However, many existing methods [21, 22, 25, 29] train the depth loss on the local region exactly on the GT center (u, v), which can lead to significant errors in object depth estimation even with slightly inaccurate object center $(\hat{u}, \hat{v})$ during inference (*i.e.*, center shifting in the image plane by a few pixels) [25].

To mitigate this issue, we train our network with an additional auxiliary head for object-wise depth estimation using the structure of [21]. Rather than solely providing depth supervision to an object center (u, v), the auxiliary head is trained with depth supervision over the entire bounding box of the object. We create the foreground object-wise depth map $\mathfrak{D} \in \mathbb{R}^{H' \times W'}$ following the policy of [43]. Then, we define the object-wise depth loss by adopting the Laplacian aleatoric uncertainty loss [9], the same as the object depth estimation task, only for the foreground regions:

$$\mathcal{L}_{obj} = \frac{1}{|\mathfrak{D}|} \sum_{z^p \in \mathfrak{D}} \frac{\sqrt{2}}{\hat{\sigma}^p} |z^p - \hat{z}^p| + \log(\hat{\sigma}^p), \qquad (7)$$

where z^p, $\hat{z}^p$ and $\hat{\sigma}^p$ are the corresponding GT object depth, prediction, and uncertainty of each pixel, respectively. Note that the additional task head is removed after training, so the proposed method does not increase the inference time.

Total loss.   The total loss $\mathcal{L}_{total}$ combines the loss used in 3D object detection baselines $\mathcal{L}_{baseline}$, the quasi-isometric loss $\mathcal{L}_{qi}$, and the object-wise depth map loss $\mathcal{L}_{obj}$ as follows:

$$\mathcal{L}_{total} = \mathcal{L}_{baseline} + \lambda_{qi} \cdot \mathcal{L}_{qi} + \lambda_{obj} \cdot \mathcal{L}_{obj}, \qquad (8)$$

where λ_{qi} and λ_{obj} represent the balancing weights for the quasi-isometric loss and the object-wise depth map loss, respectively. These values are set to 0.5 and 1. This total loss is applied to each baseline in our experiments, which we denote as "[Baseline] + Ours", as discussed further in Sec. 5.

Table 1: Evaluation results on KITTI *validation* set. (Blue/Red (positive/negative): relative performance from baseline.)

Extra data	Method	Car, $AP_{3D|R40}$ ↑			Car, $AP_{BEV|R40}$ ↑		
		Easy	Moderate	Hard	Easy	Moderate	Hard
LiDAR	DID-M3D [29]	23.93	16.22	13.98	32.65	23.15	19.48
	DID-M3D + Ours	24.77 (+3.5%)	17.12 (+5.5%)	14.30 (+2.3%)	34.32 (+5.1%)	23.45 (+1.3%)	20.64 (+6.0%)
None	MonoDLE [25]	17.32	14.35	12.22	24.62	20.25	17.75
	MonoDLE + Ours	21.31 (+23.0%)	16.53 (+15.2%)	13.93 (+14.0%)	29.34 (+19.2%)	22.27 (+10.0%)	19.20 (+8.2%)
	GUP-Net [24]	22.10	16.17	14.18	30.67	22.79	19.64
	GUP-Net + Ours	24.21 (+9.5%)	17.82 (+10.2%)	15.01 (+5.9%)	32.38 (+5.6%)	23.61 (+3.6%)	21.20 (+7.9%)
	MonoCon [21]	23.03	17.84	15.37	32.97	24.13	20.90
	MonoCon + Ours	27.90 (+21.1%)	19.43 (+8.9%)	16.92 (+10.3%)	36.15 (+9.8%)	26.15 (+8.6%)	22.56 (+7.9%)

Additionally, to simplify the implementation of our proposed (K, B, ϵ)-quasi-isometric loss, we detail the loss function in Alg.1.

4 Experiments

Datasets. The KITTI dataset [12] consists of 7,481 training images and 7,518 test images for official KITTI 3D object detection evaluation and contains three categories: *Car*, *Pedestrian*, and *Cyclist*. For additional experiments, we follow [25], which splits the training images into 3,712 and 3,769 images for training and validation sets, respectively. The Waymo dataset [34] is a recently released dataset comprising 798 training sequences and 202 validation sequences, with four categories: *Vehicles*, *Pedestrians*, *Cyclists*, and *Signs*. We use the split reported in [30], including 52,386 training and 39,848 validation images, to evaluate performance on the Waymo dataset.

Evaluation Metrics. We adhere to the protocol reported in [12] and [30] for KITTI and Waymo datasets, respectively. The KITTI 3D object detection performance is evaluated by the average precision of 3D bounding boxes ($AP_{3D|R40}$) with IoU thresholds of 0.7 for *Car* and 0.5 for *Pedestrian* and *Cyclist*. The evaluation is split into three levels of difficulty: Easy, Moderate, and Hard, based on the 2D bounding box height, occlusion level, and truncation. In contrast, the evaluation metrics of the Waymo dataset are based on 3D IoU with mean average precision (3D mAP) and mean average precision weighted by heading (3D mAPH). Each object is divided into one or two levels and evaluated at three distances: [0, 30), [30, 50), and [50, ∞) meters.

Implementation details. First, we incorporate our method into four different baselines, including CenterNet-based frameworks [21, 24, 25, 29] for the KITTI dataset. For the Waymo dataset, we choose [21], as it performs best on the KITTI dataset among our baselines. We primarily follow the experimental setup details (*i.e.*, epochs, optimizer) of each paper [21, 24, 25, 29] for a fair comparison. We denote the plugged versions of baselines as "[Baseline] + Ours". As an exception, we set all batch sizes to 16 for the KITTI and Waymo benchmarks. We retrain all baselines on the KITTI/Waymo *validation* set with "*Car*" and "*Vehicle*" classes, respectively. For the (K, B, ϵ)-quasi-isometric loss, we use $K = 1.5, B = 0.5, \epsilon = 10.0, d_1(\cdot, \cdot) = |\cdot, \cdot|, d_2(\cdot, \cdot) = \|\cdot, \cdot\|_2$ for all experiments. We provide more detailed experimental setups for each baseline in the supplementary materials.

5 Experimental Results

5.1 Evaluation Results on KITTI and Waymo Datasets

KITTI dataset. We demonstrate the effectiveness of our method on both the KITTI validation and test datasets. As shown in Tab. 1, our method can be widely applied to various baselines and significantly enhances performance by a considerable margin. Particularly, the improvement is more pronounced in models that do not utilize extra data, surpassing models that do (13.1% vs. 3.8%). We surmise that the model trained with additional LiDAR data learns more discriminative features regarding depths than the method without extra data. Notably, the performance of "MonoCon + Ours" exceeds that of models trained with additional LiDAR data. This result illustrates that our proposed metric learning method empowers MonoCon to extract depth-discriminative features without the need for extra data. Similar trends are observable in the evaluation with the KITTI test datasets, as shown in Tab. 2. The experiments demonstrate that our proposed method enhances depth discrimination not

Table 2: Evaluation results on KITTI **test** set.

Extra data	Method	Car, $AP_{3D|R40}$ ↑			Ped., $AP_{3D|R40}$ ↑			Cyc., $AP_{3D|R40}$ ↑		
		Easy	Mod.	Hard	Easy	Mod.	Hard	Easy	Mod.	Hard
LiDAR	DID-M3D [29]	24.40	16.29	13.75	-	-	-	-	-	-
	DID-M3D + Ours	27.04	16.42	13.37	14.41	9.05	8.05	4.86	3.11	2.97
	Improvement	(+10.8%)	(+0.8%)	(−2.8%)	-	-	-	-	-	-
None	MonoDLE [25]	17.23	12.26	10.29	9.64	6.55	5.44	4.59	2.66	2.45
	MonoDLE + Ours	22.11	15.30	12.72	11.75	7.80	6.29	6.02	4.12	3.42
	Improvement	(+28.3%)	(+24.8%)	(+23.6%)	(+21.9%)	(+19.1%)	(+15.6%)	(+31.2%)	(+54.9%)	(+39.6%)
	GUPNet [24]	20.11	14.20	11.77	14.72	9.53	7.87	4.18	2.56	2.09
	GUPNet + Ours	23.19	15.78	13.02	14.23	9.03	8.06	5.68	3.61	3.13
	Improvement	(+15.3%)	(+11.1%)	(+10.6%)	(−3.3%)	(−5.2%)	(+2.4%)	(+35.9%)	(+41.0%)	(+49.8%)
	MonoCon [21]	22.50	16.46	13.95	13.10	8.41	6.94	2.80	1.92	1.55
	MonoCon + Ours	23.31	16.36	13.73	14.90	10.28	8.70	5.38	2.89	2.83
	Improvement	(+3.6%)	(−0.6%)	(−1.6%)	(+13.7%)	(+22.2%)	(+25.4%)	(+92.1%)	(+50.5%)	(+82.6%)

Table 3: Evaluation results on Waymo **validation** set.

Difficulty	Method	Vehicle, AP_{3D} ↑				Vehicle, APH_{3D} ↑			
		Overall	0-30 m	30-50m	50m-∞	Overall	0-30 m	30-50 m	50 m-∞
LEVEL_1	MonoCon [21]	2.30	6.66	0.67	0.02	2.29	6.62	0.66	0.02
	MonoCon + Ours	2.50	7.62	0.72	0.02	2.48	7.57	0.72	0.02
(IOU = 0.7)	*Improvement*	(+8.7%)	(+14.4%)	(+7.5%)	(+0.0%)	(+8.3%)	(+14.4%)	(+9.1%)	(+0.0%)
LEVEL_2	MonoCon	2.16	6.64	0.64	0.02	2.15	6.59	0.64	0.02
	MonoCon + Ours	2.34	7.59	0.70	0.02	2.33	7.54	0.69	0.02
(IOU = 0.7)	*Improvement*	(+8.3%)	(+14.3%)	(+9.4%)	(+0.0%)	(+8.4%)	(+14.4%)	(+7.8%)	(+0.0%)
LEVEL_1	MonoCon	10.07	27.47	3.84	0.16	9.99	27.26	3.81	0.16
	MonoCon + Ours	10.14	28.51	3.99	0.17	10.06	28.28	3.96	0.17
(IOU = 0.5)	*Improvement*	(+0.7%)	(+3.8%)	(+3.9%)	(+6.3%)	(+0.7%)	(+3.7%)	(+3.9%)	(+6.3%)
LEVEL_2	MonoCon	9.44	27.37	3.71	0.14	9.37	27.17	3.68	0.14
	MonoCon + Ours	9.50	28.40	3.85	0.15	9.43	28.18	3.82	0.15
(IOU = 0.5)	*Improvement*	(+0.6%)	(+3.8%)	(+3.8%)	(+7.1%)	(+0.6%)	(+3.7%)	(+3.8%)	(+7.1%)

only for *Car* but also for *Pedestrian* and *Cyclist*. The average performance increases for these object categories are 10.3%, 12.4%, and 53.1%, respectively.

Waymo dataset. We extend the evaluations to the Waymo dataset to further demonstrate the generality of our method, as shown in Tab. 3. The results indicate that our proposed method consistently enhances performance by an average of 4.6% and 4.5% in terms of mAP and mAPH metrics across all levels, IoU thresholds, and distance ranges. Significantly, the proposed loss boosts the depth discrimination not only within specific depth ranges but across all depth ranges. This underscores the effectiveness of our method not just on the KITTI dataset, but on the Waymo dataset as well.

5.2 Additional Experiments

Ablation studies. To demonstrate the effectiveness of our proposed method, we conduct the ablation studies of two components of our method: (K, B, ϵ)-quasi-isometric loss $\mathcal{L}_{qi}$ and object-wise depth map loss $\mathcal{L}_{obj}$. We employ DID-M3D [29] and MonoCon [21] as baselines of a method with and without extra data. The results in Tab. 4 indicate that any method incorporating either the quasi-isometric or object-wise depth losses sees a performance improvement. Notably, the (K, B, ϵ)-quasi-isometric loss contributes to a larger performance gain than the object-wise depth loss (+2.3% vs. +1.9% for DID-M3D and +8.7% vs. +5.0% for MonoCon). The models trained with both of the proposed losses significantly surpass the performance of the baselines.

Comparison of our method with SupCR. To demonstrate the advantage of our quasi-isometric loss over existing metric learning schemes, we compare the task performance of our method with that of SupCR (Supervised Contrastive Regression) [42]. SupCR is the first regression-aware representation learning method that effectively applies metric learning to regression tasks using GT labels. Similar to our quasi-isometric loss $\mathcal{L}_{qi}$, SupCR selectively chooses the relative negative pair object features based on positive pair distance. In Tab. 5, we report the $AP_{3D|R40}$ for *Car, Moderate* and errors between the GT and prediction of four key tasks that determine the location of the 3D bounding box: $t \in z, (h, w, l), \gamma, c$, independently. The errors include the absolute difference E_z, E_{dim} for $z, (h, w, l)$, respectively, the mean angular distance $\Delta\gamma$ [11] for γ, and the accuracy $Acc._c$ for object

Table 4: Ablation studies on KITTI *validation* set.

| Components | | Baseline | Car, $AP_{3D|R40}$ ↑ | | | Overall |
$\mathcal{L}_{qi}$	$\mathcal{L}_{obj}$		Easy	Moderate	Hard	
		DID-M3D [29]	23.93	16.22	13.98	0.0%
√			24.61 (+2.8%)	16.57 (+2.2%)	14.23 (+1.8%)	+2.3%
	√		24.53 (+2.5%)	16.84 (+3.8%)	13.87 (−0.8%)	+1.8%
√	√		24.77 (+3.5%)	17.12 (+5.5%)	14.30 (+2.3%)	+3.8%
		MonoCon [21]	23.03	17.84	15.37	0.0%
√			27.00 (+17.2%)	18.68 (+4.7%)	16.02 (+4.2%)	+8.7%
	√		24.90 (+8.1%)	18.65 (+4.5%)	15.73 (+2.3%)	+5.0%
√	√		27.90 (+21.1%)	19.43 (+8.9%)	16.92 (+10.3%)	+13.5%

Table 5: Comparison of our method with SupCR on KITTI *validation* set.

Baseline	$AP_{3D|R40}$ ↑	E_z (m) ↓	E_{dim} (m) ↓	$\Delta\gamma$ (rad) ↓	$Acc._c$ (%) ↑
MonoCon [21]	17.84	0.019	0.025	$\pi/371.79$	93.15
MonoCon + SupCR	17.55 (−1.6%)	0.014 (−26.3%)	0.031 (+24.0%)	$\pi/312.78$ (+18.9%)	91.11 (−2.2%)
MonoCon + $\mathcal{L}_{qi}$	18.68 (+4.7%)	0.011 (−42.1%)	0.024 (−4.0%)	$\pi/368.11$ (+1.0%)	93.07 (−0.1%)

classification c. The results illustrate that our method enhances 3D object detection performance, whereas SupCR diminishes it. Interestingly, both methods reduce depth errors E_z as they train the encoder to extract more depth-discriminative features. However, SupCR significantly increases the errors in bounding box size and angle estimation $E_{dim}, \Delta\gamma$ by approximately 24.0% and 18.9%, respectively. It demonstrates that SupCR, which forcibly arranges the feature manifold, can negatively impact the performance of other tasks due to the complex shared representations across multiple sub-tasks.

Scalability of our quasi-isometric loss with the anchor-based method and BEV paradigm. In Tab. 1-4, we note that our method improves performance when applied to CenterNet-based baselines (anchor-free). We further demonstrate the effectiveness of the proposed metric learning incorporated into anchor-based methods and the bird-eye-view (BEV) paradigm: MonoDTR [15] and ImVoxelNet [32]. The object-wise depth map loss is not applied to these baselines, since it already uses an auxiliary depth loss or inherent nature of the BEV paradigm.

As shown in Tab. 6, although the performance enhancement compared to anchor-free methods is not as significant, our quasi-isometric loss still shows consistent improvements across all metrics for each baseline. These results suggest that the loss has broad applicability to the tasks that extract object features on image spatial coordinates given object depth labels.

Model performance with respect to the ratio of property-violated objects. The proposed quasi-isometric loss is designed to arrange the feature space in accordance with object depth labels, aiming to meet quasi-isometric properties. To demonstrate the correlation between 3D object detection performance and the ratio of features that satisfy the quasi-isometric condition, we conduct an additional experiment. In Fig. 2, we plot the ratio of object pairs violating the properties (where the Ratio = $(|\mathbf{P}^+|+|\mathbf{P}^-|)/|\mathbf{P}|$, $|\mathbf{P}| = \binom{L}{2}$, and L is the total number of objects in the dataset.) and model performance in relation to various loss scales λ_{qi}. For this exper-

Figure 2: Loss scale (log-scaled) with respect to property-violated pairs ratio and performance.

iment, we use the baseline model [21] trained with different loss scales $[10^{-5}, 10^{-3}, 10^{-2}, 10^{-1}, 0.5]$. We measure the AP_{3D} with IoU thresholds of 0.7 for *Car, Moderate* on the KITTI validation dataset. The results indicate that an increase in the loss scale corresponds with a decrease in the ratio of object pairs violating the quasi-isometric properties, leading to an improvement in model performance. This
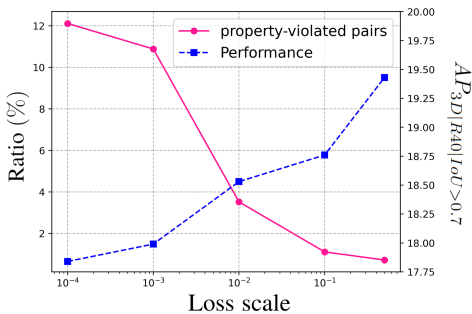
Table 6: Evaluation results of anchor-based and bird-eye-view paradigms on KITTI *validation* set.

| Method | Car, $AP_{3D|R40}\uparrow$ | | | Overall |
	Easy	Moderate	Hard	
MonoDTR [15]	24.57	18.45	15.37	-
MonoDTR + Ours	26.17 (+6.5%)	19.07 (+3.4%)	15.93 (+3.6%)	+4.5%
ImVoxelNet [32]	24.54	17.80	15.87	-
ImVoxelNet + Ours	26.14 (+8.0%)	18.20 (+7.2%)	15.81 (+3.8%)	+6.3%

Table 7: Performance of KITTI *validation* with respect to K, B, ϵ.

| Components | | | Car, $AP_{3D|R40}\uparrow$ | | | Overall |
K	B	ϵ	Easy	Moderate	Hard	
MonoCon (w/o $\mathcal{L}_{obj}$)			23.03	17.84	15.37	+0.0%
1.0	0.5	10.0	24.67 (+7.1%)	18.09 (+1.4%)	15.34 (−0.2%)	+2.8%
1.5	0.5	10.0	**27.00** (+17.2%)	18.68 (+4.7%)	**16.02** (+4.2%)	**+8.7%**
2.0	0.5	10.0	23.34 (+1.3%)	17.44 (−2.2%)	14.80 (−3.7%)	-1.5%
1.5	0.0	10.0	24.54 (+6.6%)	18.01 (+1.0%)	15.37 (+0.0%)	+2.5%
1.5	1.0	10.0	25.49 (+10.7%)	**18.70** (+4.8%)	15.82 (+2.9%)	+6.1%
1.5	5.0	10.0	23.70 (+2.9%)	18.00 (+0.9%)	15.12 (+-1.6%)	+0.9%
1.5	0.5	1.0	24.71 (+7.3%)	17.84 (+0.0%)	15.43 (+0.4%)	+2.6%
1.5	0.5	5.0	24.99 (+8.5%)	18.23 (+2.2%)	15.80 (+2.8%)	+4.5%
1.5	0.5	∞	22.85 (−0.8%)	16.91 (−5.2%)	14.14 (−8.0%)	-4.7%

suggests a potential relationship between the reduction in the ratio of property-violated object pairs and the enhancement of model performance.

Influence of hyperparameters (K, B, ϵ) **in quasi-isometric loss.** The choice of the tunable hyperparameter ϵ is crucial. An excessively small ϵ would sample a few objects within a mini-batch, making representation learning infeasible. On the other hand, quasi-isometric properties with too large an ϵ would harm the non-linearity of the feature manifold in **P**-space. To investigate the influence of hyperparameters on our quasi-isometric loss, we evaluate the performance of "Monocon + Ours" using KITTI [12] validation set for various hyperparameters (K, B, ϵ), as presented in Tab. 7. Although most hyperparameter combinations improved performance, there are notable exceptions, especially when $K = 2.0$ and $\epsilon = \infty$. We observe a decline in performance with excessively large values of K or ϵ, which define the criteria for property violation and the non-linearity of the feature manifold.

6 Conclusion

In this paper, we address the challenge of monocular 3D object detection in RGB images by proposing a novel metric learning scheme. Our method, which does not rely on extra parameters, modules, or data, concentrates on extracting depth-discriminative features without increasing the inference time or model size. By employing a distance-preserving function and the (K, B, ϵ)-quasi-isometric loss, we successfully arrange the feature space manifold in accordance with ground-truth object depth, while preserving the non-linearity of the natural feature manifold. Furthermore, by introducing an auxiliary head for object-wise depth estimation, we improve object depth quality without increasing inference time. Our experimental results on the KITTI and Waymo datasets illustrate consistent performance enhancements across different baselines, highlighting the effectiveness of our proposed method. As a potential avenue for future work, our method could feasibly be extended to multi-camera 3D object detection scenarios and other regression tasks that involve multiple sub-tasks.

Acknowledgments and Disclosure of Funding

A   General Notations

In Tab. 8, we provide a comprehensive summary of the general notations used throughout the paper to illustrate our framework and clarify the formulation of our methodology.

Table 8: General notations

Datasets	
Image	$\mathbf{I}\ :\ \mathbb{R}^{3\times H\times W}$
i-th image	$\mathbf{I}^i\ :\ \mathbb{R}^{3\times H\times W}$
Image set in mini-batch	$\mathbf{I}_b\ :\ \mathbb{R}^{B\times 3\times H\times W}$
Camera intrinsic matrix	$\mathbf{K}$
Coarse projected 3D center	(u,v)
Object depth	z
Center offset	$(\delta u, \delta v)$
3D size dimensions	(h,w,l)
Heading direction	γ
Number of training images	M
Number of objects in $\mathbf{I}^i$	N^i
Number of objects in entire images	L

Sets, States	
Task set	$\mathbf{T} = \{t_c, t_u, t_v, t_{\delta u}, t_{\delta v}, t_z, t_h, t_w, t_l, t_\gamma\} \ni t$
Image index set	$I = \{1, 2, \ldots, M\}$
object index set in image $\mathbf{I}^i$	$J = \{1, 2, \ldots, N^i\}$
Feature maps (hidden state)	$\mathbf{h}\ :\ \mathbb{R}^{C\times H'\times W'}$
Per-pixel output maps	$\tilde{\mathbf{o}}_{\mathbf{T}}\ :\ \mathbb{R}^{|\mathbf{T}|\times H'\times W'}$
Object-wise output (prediction)	$\mathbf{o}_{\mathbf{T}}\ :\ \mathbb{R}^{|\mathbf{T}|\times N^i}$
Object descriptor	$\rho\ :\ \mathbb{R}^{C\times 1\times 1}$
Distance metric	$d(\cdot, \cdot)$
Object descriptor metric space	$(\mathbf{P}, d) \equiv \mathbf{P}\text{-space}$
Object depth metric space	$(\mathbf{Z}, d) \equiv \mathbf{Z}\text{-space}$

Network components, Function	
Feature extractor	$\mathcal{F}_\theta(\cdot)\ :\ \mathbb{R}^{3\times H\times W} \to \mathbb{R}^{C\times H'\times W'}$
Task-specific lightweight head	$\mathcal{G}_{\phi^t}(\cdot)\ :\ \mathbb{R}^{C\times H'\times W'} \to \mathbb{R}^{H'\times W'}$
Extract function	$\mathcal{H}(\cdot)\ :\ \mathbb{R}^{|\mathbf{T}|\times H'\times W'} \to \mathbb{R}^{|\mathbf{T}|\times N^i}$
Quasi-isometry	$\mathcal{Q}(\cdot)\ :\ \mathbb{R} \to \mathbb{R}^C$

B   Theoretical analysis

This section provides our theoretical analysis of the proposed (K, B, ϵ)-quasi-isometric loss term, which leverages the quasi-isometric properties between two metric spaces. This analysis clarifies how our method alleviates the bottleneck task (*i.e.*, object depth estimation) through mathematical theorems and empirical observations. Ideally, we aim for the quasi-isometric loss, with real finite data points on $\mathbf{P}$-space, to function similarly to its continuous counterpart $\mathcal{M}$ (*a.k.a.* True manifold). Essentially, as the number of object feature data points $|\mathbf{P}|$ approach to ∞, we intend for the object feature set $\mathbf{P}$ originating from backbone $\mathcal{F}_\theta$ to continue to fulfill the revised quasi-isometric properties, regardless of the particular sample, in a probabilistic sense.

Fig. 2 in our main manuscript presents empirical demonstrations that, when applying the proposed quasi-isometric loss with adequate weight term λ_{qi}, the ratio of property-violated object features converges to zero. Hence, we suppose that the network trained with quasi-isometric loss consistently produces the object features that adhere to the revised quasi-isometric properties. Moreover, we observe that hyperparameters B and ϵ associated with our quasi-isometric loss term should be small enough as the number of data points in the $\mathbf{P}$-space incrementally approaches infinity. In this section,

we define the **pseudo-geodesic** to approximate the geodesic on the true manifold. We further establish that the feature space, which satisfies the local quasi-isometric properties, also adheres to the global quasi-isometric properties. Notably, in this context, the distance metric of the **P**-space is substituted by the pseudo-geodesic.

B.1 Pseudo-geodesic

The search for the true geodesic on **P**-space manifold is impeded by the discontinuous finite data points in the set **P**, rendering the true manifold unobservable. Therefore, we establish the pseudo-geodesic $\hat{\mathcal{G}}(\rho_s, \rho_t)$ to approximate the length of the shortest curve between two data points ρ_s, ρ_t on a feature manifold. This pseudo-geodesic is defined by partitioning the interval $[z_s, z_t] \subset \mathbb{R}$, denoted by $\mathcal{P}$, as follows:

$$
\hat{\mathcal{G}}(\rho_s, \rho_t) = \sum_{i=1}^{n} \|\rho_{i-1}, \rho_i\|_p,
$$
$$
\mathcal{P}_{\mathbf{P}} = (\rho_0, \rho_1, \dots, \rho_n), \ \mathcal{P}_{\mathbf{Z}} = (z_0, z_1, \dots, z_n), \tag{9}
$$
$$
\text{s.t. } z_s = z_0 < z_1 < z_2 < \cdots < z_n = z_t,
$$
$$
\max\{|z_{i-1} - z_i| : i = 1, 2, \dots, n\} \le \delta < \epsilon,
$$

where $\mathcal{P}_{\mathbf{P}}$ is the sequence of data points in $|\mathbf{P}|$-space that corresponds to partition $\mathcal{P}_{\mathbf{Z}}$, n is the number of the pseudo-geodesic $\mathcal{P}_{\mathbf{P}}$ curve segments, and δ is a sufficiently small scalar that ensures each curve segment length in $\mathcal{P}_{\mathbf{P}}$ is smaller than ϵ. Note that $\mathcal{P}_{\mathbf{Z}}$ is a subset of $\{z \in \mathbf{Z} | z_s \le z \le z_t\}$, because pseudo-geodesic should represent the shortest path between ρ_s and ρ_t. Given that the mesh of $\mathcal{P}_{\mathbf{Z}}$ is less than δ, the pseudo-geodesic should remain close to the true manifold so as δ converges to zero, thereby approximating the length of the true geodesic. The defined pseudo-geodesic metric for any arbitrary object feature pair (ρ_1, ρ_2) in **P**-space satisfies the properties of a distance metric.

Definition B.1 (Quasi-isometric Properties), Let $\mathcal{Q}$ represent a function that maps one metric space (M_1, d_1) to another metric space (M_2, d_2). $\mathcal{Q}$ is termed a quasi-isometry from (M_1, d_1) to (M_2, d_2) if there exist constants $K \ge 1$, $B \ge 0$, and $\epsilon \ge 0$ such that the following two properties are satisfied:

(i) $\forall x_1, x_2 \in M_1 : \frac{1}{K} d_1(x_1, x_2) - B \le d_2(\mathcal{Q}(x_1), \mathcal{Q}(x_2)) \le K d_1(x_1, x_2) + B$.

(ii) $\forall z \in M_2 : \exists x \in M_1 \text{ s.t. } d_2(z, \mathcal{Q}(x)) \le \epsilon$.

Definition B.2 (Local Quasi-isometric Properties), Local quasi-isometry refers to a function whereby any two neighboring points (x_1, x_2) in the domain set M_1 comply with the **Definition B.1**, with $x_2 \in \mathcal{B}_{x_1, \epsilon}$. Let $\mathcal{Q}$ be a function from one metric space (M_1, d_1) to another metric space (M_2, d_2). $\mathcal{Q}$ is considered a quasi-isometry from (M_1, d_1) to (M_2, d_2) if there exist constants $K \ge 1$, $B \ge 0$, and $\epsilon \ge 0$ that satisfy the following conditions:

(i) $\mathbf{U}_{\acute{x}} = \{x \in M_1 | x \in \mathcal{B}_{\acute{x}, \epsilon}\}$, where $\acute{x} \in M_1$.

(ii) $\forall x_1 \in M_1$, s.t. $\forall x_2 \in \mathbf{U}_{x_1} : \frac{1}{K} d_1(x_1, x_2) - B \le d_2(\mathcal{Q}(x_1), \mathcal{Q}(x_2)) \le K d_1(x_1, x_2) + B$,

(iii) $\forall z \in M_2 : \exists x \in M_1$, s.t. $d_2(z, \mathcal{Q}(x)) \le \epsilon$.

Theorem. *Given that $B = B'/|\mathbf{P}|$ and $B' \ge 0$, the two metric spaces $(\mathbf{Z}, |\cdot, \cdot|)$ and $(\mathbf{P}, \hat{\mathcal{G}}(\cdot, \cdot))$ are quasi-isometric.*

Proof. Let $(\mathbf{Z}, |\cdot, \cdot|)$ and $(\mathbf{P}, \|\cdot, \cdot\|_p)$ be two metric spaces. Assume that for all $(z_i, z_j) \in \mathbf{Z} \times \mathbf{Z}$ and $(\rho_i, \rho_j) \in \mathbf{P} \times \mathbf{P}$, the local quasi-isometric properties defined in **Definition B.2** are satisfied. We need to show that these pairs also satisfy the **Definition B.1** when the distance metric of **P**-space is the pseudo-geodesic $\hat{\mathcal{G}}$. We proceed as follows:

$$
\frac{1}{K} |z_{i-1} - z_i| - B \le \|\rho_{i-1}, \rho_i\|_p \le K |z_{i-1} - z_i| + B \qquad \text{(by \textbf{Definition B.2})}
$$

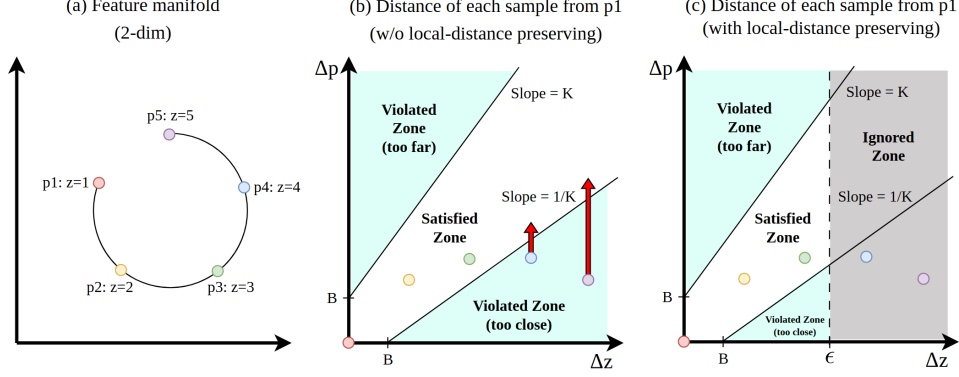Since this inequality holds for all i, summing over all i from 1 to $|\mathcal{P}_{\mathbf{Z}}|$, we have

Figure 3: Example of non-linearity preservation by using local-constraint.

$$\sum_{i=1}^{|\mathcal{P}_{\mathbf{z}}|} \left(\frac{1}{K}|z_{i-1} - z_i| - B \right) \leq \sum_{i=1}^{|\mathcal{P}_{\mathbf{z}}|} \|\rho_{i-1}, \rho_i\|_p \leq \sum_{i=1}^{|\mathcal{P}_{\mathbf{z}}|} (K|z_{i-1} - z_i| + B)$$

$$\Longrightarrow \sum_{i=1}^{|\mathcal{P}_{\mathbf{z}}|} \left(\frac{1}{K}|z_{i-1} - z_i| - B \right) \leq \hat{\mathcal{G}}(\rho_s, \rho_t) \leq \sum_{i=1}^{|\mathcal{P}_{\mathbf{z}}|} (K|z_{i-1} - z_i| + B) \qquad \text{(by Eq. 9)}$$

$$\Longrightarrow \frac{1}{K}|z_s - z_t| - |\mathcal{P}_{\mathbf{z}}|B \leq \hat{\mathcal{G}}(\rho_s, \rho_t) \leq K|z_s - z_t| + |\mathcal{P}_{\mathbf{z}}|B \qquad \text{(by Eq. 9)}$$

$$\Longrightarrow \frac{1}{K}|z_s - z_t| - |\mathbf{P}|B \leq \hat{\mathcal{G}}(\rho_s, \rho_t) \leq K|z_s - z_t| + |\mathbf{P}|B \qquad (\because |\mathcal{P}_{\mathbf{z}}| \leq \mathbf{P})$$

$$\Longrightarrow \frac{1}{K}|z_s - z_t| - B' \leq \hat{\mathcal{G}}(\rho_s, \rho_t) \leq K|z_s - z_t| + B' \qquad (\because B = \frac{B'}{|\mathbf{P}|})$$

$$\Longrightarrow (\mathbf{Z}, |\cdot, \cdot|) \underset{q.i.}{\sim} (\mathbf{P}, \hat{\mathcal{G}}(\cdot, \cdot))$$

$\blacksquare$

The distance metric defined as $\hat{\mathcal{G}}(\cdot, \cdot)$ satisfies all axioms of a distance function, and two metric spaces $(\mathbf{Z}, |\cdot, \cdot|), (\mathbf{P}, \hat{\mathcal{G}}(\cdot, \cdot))$ conform to the properties in **Definition B.1** with respect to (K, B', ϵ). This theorem implies that, by establishing an appropriate B with respect to the number of objects in the entire dataset, the local quasi-isometric properties roughly preserve the pseudo-geodesic distance as opposed to the Minkowski distance on $\mathbf{P}$-space. This is analogous to stating that the pseudo-geodesic between two arbitrary points ρ_s, ρ_t on $\mathbf{P}$-space is uniformly close to $|z_s - z_t|$.

B.2 Non-linearity preservation

The proposed quasi-isometric loss benefits from the incorporation of a local distance-preserving condition. This ensures a structured arrangement of the feature manifold while maintaining its intricate overall shape. For instance, suppose that there is the feature space being modeled by a subset of the circle manifold, as depicted in Fig. 3-(a). From a depth perspective, this manifold represents a structured feature space since the distance of all object feature pairs along the geodesic corresponds closely with depth distance. However, without the local distance-preserving condition, as shown in Fig. 3-(b), the quasi-isometric loss might erroneously infer that features $p4$ and $p5$ violate property norms.

On the other hand, integrating the local distance-preserving condition denoted by ϵ (Fig. 3) refines the quasi-isometric loss to only consider neighbor samples. This approach enables a more nuanced arrangement of the feature manifold while preserving the overall shape and non-linearity of the original feature space.

In Tab. 9, we report $AP_{3D|R40}$ for *Car, Moderate* and errors between the GT and prediction of four key tasks that determine the location of the 3D bounding box: $t \in z, (h, w, l), \gamma, c$, independently.

Table 9: Performance trade-off between *"depth"* and *"other sub-tasks"* with respect to ϵ.

Method	Performance $AP_{3D\mid R40}\uparrow$	Depth $E_z\ (m)\downarrow$	Others $E_{dim}\ (m)\downarrow$	$\Delta\gamma$ (rad) $\downarrow$	$Acc._c$ (%) $\uparrow$
MonoCon	17.84	0.019	0.025	$\pi/371.79$	93.15
MonoCon + $\mathcal{L}_{\text{SupCR}}$	17.55 (−1.6%)	0.014 (−26.3%)	0.031 (+24.0%)	$\pi/312.78$ (+18.9%)	91.11 (−2.2%)
MonoCon + $\mathcal{L}_{qi}$ ($\epsilon = 1$)	17.84 (+0.0%)	0.018 (−5.3%)	0.025 (+0.0%)	$\pi/371.21$ (+0.2%)	93.17 (+0.0%)
MonoCon + $\mathcal{L}_{qi}$ ($\epsilon = 5$)	18.23 (+2.2%)	0.013 (−31.6%)	0.025 (+0.0%)	$\pi/\mathbf{372.10}$ (−0.1%)	**93.51** (+0.4%)
MonoCon + $\mathcal{L}_{qi}$ ($\epsilon = 10$)	**18.68** (+4.7%)	0.011 (−42.1%)	**0.024** (−4.0%)	$\overline{\pi/368.11}$ (+1.0%)	93.07 (−0.1%)
MonoCon + $\mathcal{L}_{qi}$ ($\epsilon = 20$)	18.12 (+1.6%)	0.011 (−42.1%)	0.026 (+4.0%)	$\pi/366.19$ (+1.5%)	92.00 (−1.2%)
MonoCon + $\mathcal{L}_{qi}$ ($\epsilon = \infty$)	16.91 (−0.9%)	**0.010** (−47.4%)	0.028 (+12.0%)	$\pi/367.92$ (+1.1%)	91.83 (−1.4%)

The empirical results illustrate that our method with excessively small or high ϵ would sample a few objects within a mini-batch, making representation learning infeasible, or harming the non-linearity of the feature manifold in $\mathbf{P}$-space, respectively.

C More detailed experimental setups

Table 10: Experimental setup of each baseline (horizontal flip: hf, random crop: rc, scaling: s, photometric distortion: pd, random shifting: rs).

baseline	batch	epoch	image resolution	optimizer	augmentation type
DID-M3D [29]	16	150	1280×384	Adam [17]	hf, rc, s
MonoDLE [25]	16	140	1280×384	Adam	hf, rc, s
GUPNet [24]	16	140	1280×384	Adam	hf, rc, s
MonoCon [21]	16	200	1248×384	AdamW [23]	hf, pd, rs
MonoCon [21](Waymo [34])	16	50	768x512	AdamW	hf, pd, rs
MonoDTR [15]	16	120	1280×288	Adam	hf

As mentioned in the paper, our experimental settings are the same as the respective baselines except for the batch size. We elaborate on the specifics of the experimental setup in Tab. 10. For all baselines, we use DLA, DLAUp [41] as the backbone and neck, respectively. We impose our quasi-isometric loss and object-wise depth map loss using the output feature extracted from DLAUp. When computing the quasi-isometric loss, we first apply a 5x5 average pooling to the output feature prior to the extraction of the object descriptor. This extracted object descriptor is subsequently utilized to compute the loss. Regarding the object-wise depth map loss, we abide by the lightweight head structure adopted in each baseline and introduce an additional head. The output feature derived from DLAUp serves as the input, and the object-wise depth map is generated as the output. This depth map forms the basis for the computation of the loss.

D Qualitative results on KITTI dataset

We provide additional qualitative results using the MonoCon and "MonoCon + Ours" as discussed in Tab. 1 of the main manuscript, utilizing the KITTI *validation* set. In Fig. 4, we showcase the predictions of "MonoCon + Ours" in the image view on the left, while on the right, we present the Bird's Eye view displaying the predictions of Monocon, "MonoCon + Ours", and the GT. Generally, the models employing our method tend to align more closely with the GT.

E Full evaluation results on KITTI *test* set

Finally, we report the full evaluation results of four baseline models [21, 24, 25, 29] on KITTI *test* set in Tab. 11-13.

Table 11: Full evaluation results of *Car* class on KITTI *test* set.

Extra data	Method	Car, $AP_{3D\|R40}$ ↑			Car, $AP_{BEV\|R40}$ ↑		
		Easy	Mod.	Hard	Easy	Mod.	Hard
LiDAR	DID-M3D [29]	24.40	16.29	13.75	32.95	22.76	19.83
	DID-M3D + Ours	27.04 (+10.8%)	16.42 (+0.8%)	13.37 (−2.8%)	34.77 (+5.5%)	22.59 (−0.7%)	19.15 (−3.4%)
None	MonoDLE [25]	17.23	12.26	10.29	24.79	18.89	16.00
	MonoDLE + Ours	22.11 (+28.3%)	15.30 (+24.8%)	12.72 (+23.6%)	30.28 (+22.1%)	20.99 (+11.1%)	17.73 (+10.8%)
	GUPNet [24]	20.11	14.20	11.77	30.29	21.19	18.20
	GUPNet + Ours	23.19 (+15.3%)	15.78 (+11.1%)	13.02 (+10.6%)	32.45 (+7.1%)	22.31 (+5.3%)	18.32 (+0.7%)
	MonoCon [21]	22.50	16.46	13.95	31.12	22.10	19.00
	MonoCon + Ours	23.31 (+3.6%)	16.36 (−0.6%)	13.73 (−1.6%)	32.37 (+4.0%)	22.73 (+2.9%)	19.81 (+4.3%)

Table 12: Full evaluation results of *Ped.* class on KITTI *test* set.

Extra data	Method	Ped, $AP_{3D\|R40}$ ↑			Ped, $AP_{BEV\|R40}$ ↑		
		Easy	Mod.	Hard	Easy	Mod.	Hard
LiDAR	DID-M3D [29]	-	-	-	-	-	-
	DID-M3D + Ours	14.41	9.05	8.05	15.70	10.20	8.62
None	MonoDLE [25]	9.64	6.55	5.44	10.73	6.96	6.20
	MonoDLE + Ours	11.75 (+21.9%)	7.80 (+19.1%)	6.29 (+15.6%)	12.85 (+19.8%)	8.75 (+25.7%)	7.31 (+17.9%)
	GUPNet [24]	14.72	9.53	7.87	-	-	-
	GUPNet + Ours	14.23 (−3.3%)	9.03 (−5.2%)	8.06 (+2.4%)	15.50	10.16	8.65
	MonoCon [21]	13.10	8.41	6.94	-	-	-
	MonoCon + Ours	14.90 (+13.7%)	10.28 (+22.2%)	8.70 (+25.4%)	16.29	10.88	9.31

Table 13: Full evaluation results of *Cyc.* class on KITTI *test* set.

Extra data	Method	Cyc, $AP_{3D\|R40}$ ↑			Cyc, $AP_{BEV\|R40}$ ↑		
		Easy	Mod.	Hard	Easy	Mod.	Hard
LiDAR	DID-M3D [29]	-	-	-	-	-	-
	DID-M3D + Ours	4.86	3.11	2.97	5.94	4.02	3.55
None	MonoDLE [25]	4.59	2.66	2.45	5.34	3.28	2.83
	MonoDLE + Ours	6.02 (+31.2%)	4.12 (+54.9%)	3.42 (+39.6%)	8.33 (+56.0%)	5.64 (+72.0%)	4.83 (+70.7%)
	GUPNet [24]	4.18	2.56	2.09	-	-	-
	GUPNet + Ours	5.68 (+35.9%)	3.61 (+41.0%)	3.13 (+49.8%)	6.47	3.85	3.82
	MonoCon [21]	2.80	1.92	1.55	-	-	-
	MonoCon + Ours	5.38 (+92.1%)	2.89 (+50.5%)	2.83 (+82.6%)	7.07	4.06	3.85

Figure 4: Comparison of qualitative results between MonoCon and MonoCon + ours. Yellow circles highlight accurately estimated parts compared to the MonoCon.
(GT: green, Prediction of MonoCon: blue, Prediction of MonoCon + Ours: red)

References

[1] Hervé Abdi and Lynne J Williams. Principal component analysis. *Wiley interdisciplinary reviews: computational statistics*, 2(4):433–459, 2010.

[2] Mikhail Belkin and Partha Niyogi. Laplacian eigenmaps for dimensionality reduction and data representation. *Neural computation*, 15(6):1373–1396, 2003.

[3] Garrick Brazil and Xiaoming Liu. M3d-rpn: Monocular 3d region proposal network for object detection. In *ICCV*, pages 9287–9296, 2019.

[4] Stephen G Brick. Quasi-isometries and ends of groups. *Journal of pure and applied algebra*, 86(1):23–33, 1993.

[5] Shaosheng Cao, Wei Lu, and Qiongkai Xu. Deep neural networks for learning graph representations. In *AAAI*, volume 30, 2016.

[6] Ting Chen, Simon Kornblith, Mohammad Norouzi, and Geoffrey Hinton. A simple framework for contrastive learning of visual representations. In *ICML*, pages 1597–1607. PMLR, 2020.

[7] Xinlei Chen and Kaiming He. Exploring simple siamese representation learning. In *CVPR*, pages 15750–15758, 2021.

[8] Yi-Nan Chen, Hang Dai, and Yong Ding. Pseudo-stereo for monocular 3d object detection in autonomous driving. In *CVPR*, pages 887–897, 2022.

[9] Yongjian Chen, Lei Tai, Kai Sun, and Mingyang Li. Monopair: Monocular 3d object detection using pairwise spatial relationships. In *CVPR*, pages 12093–12102, 2020.

[10] Mingyu Ding, Yuqi Huo, Hongwei Yi, Zhe Wang, Jianping Shi, Zhiwu Lu, and Ping Luo. Learning depth-guided convolutions for monocular 3d object detection. In *CVPRW*, pages 1000–1001, 2020.

[11] David Eigen and Rob Fergus. Predicting depth, surface normals and semantic labels with a common multi-scale convolutional architecture. In *ICCV*, pages 2650–2658, 2015.

[12] Andreas Geiger, Philip Lenz, and Raquel Urtasun. Are we ready for autonomous driving? the kitti vision benchmark suite. In *CVPR*, 2012.

[13] Mikhael Gromov, Misha Katz, Pierre Pansu, and Stephen Semmes. *Metric structures for Riemannian and non-Riemannian spaces*, volume 152. Springer, 1999.

[14] Yu Hong, Hang Dai, and Yong Ding. Cross-modality knowledge distillation network for monocular 3d object detection. In *ECCV*, pages 87–104. Springer, 2022.

[15] Kuan-Chih Huang, Tsung-Han Wu, Hung-Ting Su, and Winston H Hsu. Monodtr: Monocular 3d object detection with depth-aware transformer. In *CVPR*, pages 4012–4021, 2022.

[16] Prannay Khosla, Piotr Teterwak, Chen Wang, Aaron Sarna, Yonglong Tian, Phillip Isola, Aaron Maschinot, Ce Liu, and Dilip Krishnan. Supervised contrastive learning. *NeurIPS*, 33:18661–18673, 2020.

[17] Diederik P Kingma and Jimmy Ba. Adam: A method for stochastic optimization. *arXiv preprint arXiv:1412.6980*, 2014.

[18] Joseph B Kruskal. Multidimensional scaling by optimizing goodness of fit to a nonmetric hypothesis. *Psychometrika*, 29(1):1–27, 1964.

[19] Abhinav Kumar, Garrick Brazil, Enrique Corona, Armin Parchami, and Xiaoming Liu. Deviant: Depth equivariant network for monocular 3d object detection. In *ECCV*, pages 664–683. Springer, 2022.

[20] Qing Lian, Botao Ye, Ruijia Xu, Weilong Yao, and Tong Zhang. Exploring geometric consistency for monocular 3d object detection. In *CVPR*, pages 1685–1694, June 2022.

[21] Xianpeng Liu, Nan Xue, and Tianfu Wu. Learning auxiliary monocular contexts helps monocular 3d object detection. In *AAAI*, volume 36, pages 1810–1818, 2022.

[22] Zechen Liu, Zizhang Wu, and Roland Tóth. Smoke: Single-stage monocular 3d object detection via keypoint estimation. In *CVPRW*, pages 996–997, 2020.

[23] Ilya Loshchilov and Frank Hutter. Decoupled weight decay regularization. *arXiv preprint arXiv:1711.05101*, 2017.

[24] Yan Lu, Xinzhu Ma, Lei Yang, Tianzhu Zhang, Yating Liu, Qi Chu, Junjie Yan, and Wanli Ouyang. Geometry uncertainty projection network for monocular 3d object detection. In *ICCV*, pages 3111–3121, 2021.

[25] Xinzhu Ma, Yinmin Zhang, Dan Xu, Dongzhan Zhou, Shuai Yi, Haojie Li, and Wanli Ouyang. Delving into localization errors for monocular 3d object detection. In *CVPR*, pages 4721–4730, 2021.

[26] Fabian Manhardt, Wadim Kehl, and Adrien Gaidon. Roi-10d: Monocular lifting of 2d detection to 6d pose and metric shape. In *CVPR*, pages 2069–2078, 2019.

[27] Arsalan Mousavian, Dragomir Anguelov, John Flynn, and Jana Kosecka. 3d bounding box estimation using deep learning and geometry. In *CVPR*, pages 7074–7082, 2017.

[28] Dennis Park, Rares Ambrus, Vitor Guizilini, Jie Li, and Adrien Gaidon. Is pseudo-lidar needed for monocular 3d object detection? In *ICCV*, pages 3142–3152, 2021.

[29] Liang Peng, Xiaopei Wu, Zheng Yang, Haifeng Liu, and Deng Cai. Did-m3d: Decoupling instance depth for monocular 3d object detection. In *ECCV*, pages 71–88. Springer, 2022.

[30] Cody Reading, Ali Harakeh, Julia Chae, and Steven L Waslander. Categorical depth distribution network for monocular 3d object detection. In *CVPR*, pages 8555–8564, 2021.

[31] Sam T Roweis and Lawrence K Saul. Nonlinear dimensionality reduction by locally linear embedding. *science*, 290(5500):2323–2326, 2000.

[32] Danila Rukhovich, Anna Vorontsova, and Anton Konushin. Imvoxelnet: Image to voxels projection for monocular and multi-view general-purpose 3d object detection. In *WACV*, pages 2397–2406, 2022.

[33] Adrian Spurr, Aneesh Dahiya, Xi Wang, Xucong Zhang, and Otmar Hilliges. Self-supervised 3d hand pose estimation from monocular rgb via contrastive learning. In *ICCV*, pages 11230–11239, 2021.

[34] Pei Sun, Henrik Kretzschmar, Xerxes Dotiwalla, Aurelien Chouard, Vijaysai Patnaik, Paul Tsui, James Guo, Yin Zhou, Yuning Chai, Benjamin Caine, et al. Scalability in perception for autonomous driving: Waymo open dataset. In *CVPR*, pages 2446–2454, 2020.

[35] Joshua B Tenenbaum, Vin de Silva, and John C Langford. A global geometric framework for nonlinear dimensionality reduction. *science*, 290(5500):2319–2323, 2000.

[36] Daixin Wang, Peng Cui, and Wenwu Zhu. Structural deep network embedding. In *Proceedings of the 22nd ACM SIGKDD international conference on Knowledge discovery and data mining*, pages 1225–1234, 2016.

[37] Yan Wang, Wei-Lun Chao, Divyansh Garg, Bharath Hariharan, Mark Campbell, and Kilian Q Weinberger. Pseudo-lidar from visual depth estimation: Bridging the gap in 3d object detection for autonomous driving. In *CVPR*, pages 8445–8453, 2019.

[38] Yaoming Wang, Yangzhou Jiang, Jin Li, Bingbing Ni, Wenrui Dai, Chenglin Li, Hongkai Xiong, and Teng Li. Contrastive regression for domain adaptation on gaze estimation. In *CVPR*, pages 19376–19385, 2022.

[39] Zizhang Wu, Yunzhe Wu, Jian Pu, Xianzhi Li, and Xiaoquan Wang. Attention-based depth distillation with 3d-aware positional encoding for monocular 3d object detection. *arXiv preprint arXiv:2211.16779*, 2022.

[40] Yu Xiang, Wongun Choi, Yuanqing Lin, and Silvio Savarese. Data-driven 3d voxel patterns for object category recognition. In *CVPR*, pages 1903–1911, 2015.

[41] Fisher Yu, Dequan Wang, Evan Shelhamer, and Trevor Darrell. Deep layer aggregation. In *CVPR*, pages 2403–2412, 2018.

[42] Kaiwen Zha, Peng Cao, Yuzhe Yang, and Dina Katabi. Supervised contrastive regression. *arXiv preprint arXiv:2210.01189*, 2022.

[43] Renrui Zhang, Han Qiu, Tai Wang, Xuanzhuo Xu, Ziyu Guo, Yu Qiao, Peng Gao, and Hongsheng Li. Monodetr: Depth-aware transformer for monocular 3d object detection. *arXiv preprint arXiv:2203.13310*, 2022.

[44] Yunpeng Zhang, Jiwen Lu, and Jie Zhou. Objects are different: Flexible monocular 3d object detection. In *CVPR*, pages 3289–3298, 2021.

[45] Zhenyue Zhang and Hongyuan Zha. Principal manifolds and nonlinear dimensionality reduction via tangent space alignment. *SIAM journal on scientific computing*, 26(1):313–338, 2004.

[46] Xingyi Zhou, Dequan Wang, and Philipp Krähenbühl. Objects as points. *arXiv preprint arXiv:1904.07850*, 2019.